THE JOURNAL OF PHYSICAL CHEMISTRY C

pubs.acs.org/JPCC

Article

First-Principles Analyses of Nanoionic Effects at Oxide–Oxide Heterointerfaces for Electrochemical Applications

Sarmad W. Saeed, Truls Norby, and Tor S. Bjørheim*

Cite This: *J. Phys. Chem. C* 2020, 124, 14072–14081

Read Online

ACCESS | Metrics & More | Article Recommendations

ABSTRACT: Defect segregation at homo- and heterointerfaces enables heterogeneous doping of functional nanocomposites for enhanced charge and mass transport or storage properties compared to homogeneously doped bulk materials. The direction and extent of interfacial defect segregation is governed by the chemical potentials of charged species in the two phases. In this contribution we show that the extent of homogeneous doping at a model heterointerface can be tuned by both materials selection and homogeneous doping of the bulk phases from first-principles calculations. Homogenous doping is found to dictate the direction of defect segregation at a heterointerface, enabling electrostatic potential differences across a model $SrTiO_3$ and $BaZrO_3$ interface in excess of 3 V. The results suggest that composites of donor-doped $SrTiO_3$ and acceptor-doped $BaZrO_3$ exhibit significant mass storage capacity, enabling use for hydrogen storage or thermochemical water splitting.

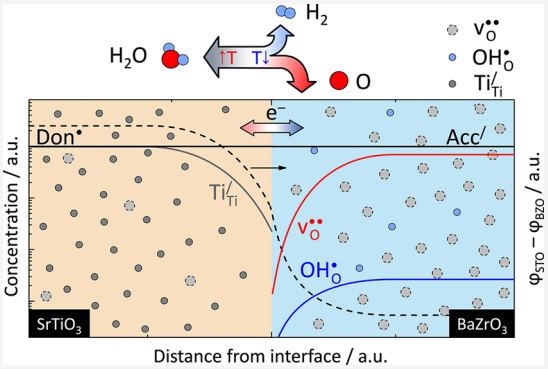

INTRODUCTION

Job-sharing by spatial decoupling of the charge-compensating and charge-transporting species in separate phases has been demonstrated as a promising strategy to tackle the demands on intercalation electrodes in rechargeable Li batteries.[1−4] The defect chemical properties of the interfacial region at heterointerfaces of chemically different materials may deviate from those of the bulk constituent phases. The defect concentration in the interfacial space-charge regions, and thus the charge and mass storage capacity of the material, may far exceed that of the individual phases.

These interfacial nanoionic effects stem from differences in the chemical potentials of charged species in constituent bulk phases, and may as such be realized in a variety of manners and tailored to a wide range of purposes. More generally, job sharing is an example of two-phase doping (or heterogeneous doping) where one phase effectively acts as a donor while the other acts as an acceptor. In contrast to a homogeneously doped bulk material, where dopants not only determine charge-carrier concentrations but also limit their mobilities,[5−7] such two-phase systems enable charge compensation and transport to be spatially separated in the two joining phases. In semiconductor physics the phenomenon is termed *modulation doping* and has been proposed as a strategy to realize high-mobility materials in heterostructures consisting of a heavily doped charge carrier injecting phase and undoped phases in which the carrier is unaffected by scattering mechanisms that limit the transport properties of doped semiconductors.[8,9]

Job sharing has furthermore been shown to drastically increase the ionic conductivity of ionic nanocomposites such as LiI containing nanoinclusions of Al_2O_3 and several halides that typically share a common cation or anion, such as AgCl/AgI and BaF_2/CaF_2 (Figure 1a).[1,2,10−14] The enhancement stems from segregation of species between the two phases, leading to increased concentration of mobile defects close to the interface. The defect chemistry of BaF_2/CaF_2 nanocomposites is for instance controlled by the thermodynamics of the heterogeneous defect reaction[13]

$$F^{\times}_{F,BaF_2} + v^{\times}_{i,CaF_2} \rightleftharpoons v^{\bullet}_{F,BaF_2} + F'_{i,CaF_2} \quad (1)$$

which thus results in significantly higher concentration of defects near the phase boundary than in the bulk regions of BaF_2 or CaF_2 (Figure 1a).

Interfaces between different materials may also serve as mass storage centers in situations where the overall stoichiometry of the composite changes.[15,16] Typically, this occurs in composites of materials having different electronic properties and defect structures, which enable job-sharing storage of chemical species. Such storage has been reported in

Received: January 15, 2020
Revised: May 18, 2020
Published: May 26, 2020

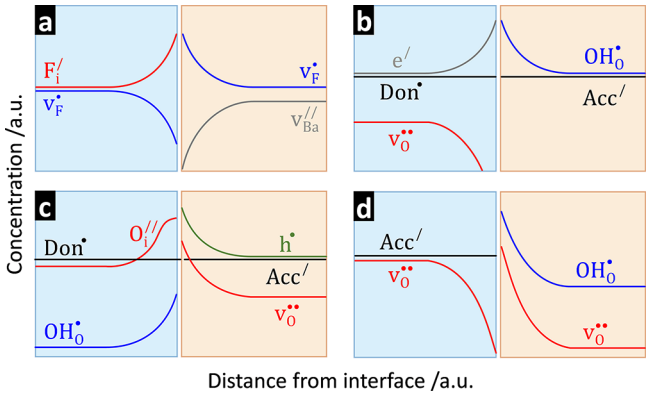

Figure 1. Different situations that may occur at interfaces between doped and undoped materials that could result in enhanced defect concentrations (a–c) and eventually enable mass storage (b and c) due to change in the stoichiometry in the near-interface region. In addition to increased defect concentration, spatial separation of transporting and charge-compensating defects (d) can result in improved electrical conductivity due to elimination of association between defects.

composites of Ru and Li_2O[4] and of Ti and LiF.[3] In both composites, the authors suggested the underlying mechanism to be job-sharing storage of Li near the interface as e^- on the metal side and Li^+ on the ionic side of the interface. The Ru/Li_2O composite has also been reported to store H_2 as e^- and/or H^- in Ru and H^+ in Li_2O.[17]

There are only a few examples of job sharing in composites consisting of ion and/or mixed conducting *oxides*.[18−22] Figure 1 illustrates how charge separation may—depending on the defect chemistry of the heterointerface—enable excess storage of chemical species such as H and O (Figure 1, parts b and c, respectively) near the interface. Besides enabling mass storage, the situations depicted in Figure 1b,c lead to enhanced mixed conductivity and may as such enable novel electrodes for fuel cells and electrolyzers as well as H_2 or O_2 gas separation membranes, in which the performance relies on ambipolar transport of ionic and electronic species. Spatial separation of the charge-compensating and transporting species may in principle also lead to enhanced transport properties by eliminating trapping effects between the dopants and charge carriers (Figure 1d). For instance, in Y-doped $BaZrO_3$, a typically observed activation energy of proton mobility is 0.45 eV, of which 0.29 eV is due to association between the proton and the Y-dopant.[6] Eliminating the association contribution could result in highly improved proton conductivity at lower temperatures.

In a recent study,[23] we established a general framework for calculations of the interface defect chemistry of oxide heterostructures, using $SrTiO_3$ and $BaZrO_3$ as a model system. We showed, through first-principles calculations, that a significant heterogeneous doping effect is expected at interfaces between 10 mol % acceptor-doped $BaZrO_3$ and acceptor-doped $SrTiO_3$. According to our calculations, $v_O^{\bullet\bullet}$ and $OH_O^{\bullet}$ are enriched in $BaZrO_3$ and depleted in $SrTiO_3$ at a coherent interface as a result of their negative energy for segregation to $BaZrO_3$. This leads to an "excess" $OH_O^{\bullet}$ concentration in $BaZrO_3$ exceeding that induced by the homogeneous Y-dopant due to the effective heterogeneous acceptor-doping effect induced by $SrTiO_3$. The electrostatic potential difference and in turn the extent of defect enrichment (or depletion) at the interface relate to the chemical potential of charged species in the two materials. The chemical potential is in turn controlled by the intrinsic chemical properties of both materials (i.e., formation energy of defects), the concentration of extrinsic defects (i.e., homogeneous doping) in the bulk phases, and strain fields in the interface. As such, a variety of defect chemical situations may be achieved at interfaces of chemically different oxides, potentially enabling nanocomposites with novel mass and charge storage and transport properties.

In this contribution, we further explore (i) the relationship between the oxides' chemistry, including homogeneous doping, on the (hetero)interface defect chemistry of oxides, (ii) size/confinement effects on the (hetero)interface defect chemistry, and (iii) implications and potential in electrochemical applications (composite electrodes and gas separation membranes) from first-principles calculations. The epitaxial (001) interfaces between acceptor-doped $BaZrO_3$ and undoped or donor-doped $SrTiO_3$ serve as a model system, in which the bulk phases are dominated by oxygen vacancies or protons, and oxygen vacancies and electrons, respectively.

COMPUTATIONAL AND THEORETICAL APPROACHES

All first-principles calculations were performed using the plane-wave DFT with the GGA-PBE[24] (for $BaZrO_3$ and $BaCeO_3$) and GGA-PBE+*U* for ($SrTiO_3$ and $BaTiO_3$) functionals as implemented in the VASP code.[25−27] In the DFT+*U* calculations, we adopt the approach introduced by Dudarev et al.[28] with an on-site repulsion of 4 eV to the Ti d-states. The *U* parameter has been determined *ab initio* according to the method in ref 29. Projector augmented wave (PAW) potentials[30,31] with valence configurations $4s^24p^65s^2$, $5s^25p^66s^2$, $3s^23p^63d^24s^2$, $4s^24p^64d^25s^2$, $5s^25p^64f^15d^16s^2$, and $2s^22p^4$ for Sr, Ba, Ti, Zr, Ce, and O, respectively, were used. A constant cutoff energy of 500 eV and convergence criteria of 10^{-4} and 10^{-8} eV, respectively, for the ionic and electronic relaxations were employed. Ground state structures were adopted for all materials except for $BaTiO_3$, for which we adopted the high temperature cubic structure as its high symmetry significantly reduces the computation time. Test calculations on cubic $SrTiO_3$ show that the choice of structure has a negligibly small effect on the calculated formation energies of defects (typically less than 0.1 eV) and electrostatic potential difference across the interface. 3 × 3 × 3 supercells of cubic ($Pm\bar{3}m$) $BaZrO_3$ and $BaTiO_3$, and 2 × 2 × 2 supercells of tetragonal ($I4/mcm$) $SrTiO_3$ and orthorhombic ($Pnma$) $BaCeO_3$ have been used for total energy calculations, using a 2 × 2 × 2 **k**-mesh that has been sampled according to the Monkhorst−Pack scheme. For calculation of vacuum potentials, supercells of 1 × 1 × 11 (for cubic materials) or 1 × 1 × 6 (for tetragonal and orthorhombic materials), with corresponding **k**-meshes of 6 × 6 × 1 or 4 × 4 × 1, were used. Slab calculations were performed on transition metal terminated surfaces with 11 (cubic) or 13 (tetragonal, orthorhombic) atom layers. The vibrational formation entropies and zero point energies were calculated with the finite displacement method as implemented in the Phonopy code,[32] using displacements of ±0.01 Å, and evaluated at the Γ-point.

The obtained total energies and calculated entropies are used to determine the free energy of defect formation after alignment with respect to the vacuum level:

https://dx.doi.org/10.1021/acs.jpcc.0c00385
J. Phys. Chem. C 2020, 124, 14072−14081

$$\Delta_f G_{def}^{\circ,aligned} = E_{def}^{el} - E_{bulk}^{el} + \Delta_f G_{def}^{vib}(T) - \sum_i \Delta n_i \mu_i(T, p) + q(\varepsilon_{VBM} + \Delta\varepsilon + IP) \quad (2)$$

Here, E_{def}^{el} and E_{bulk}^{el} are the DFT energies of a defective and a perfect supercell, while $\Delta_f G_{def}^{vib}(T)$, Δn_i, and $\mu_i(T,p)$ are the vibrational contribution to the free energy of defect formation, change in the number of elements, i, upon defect formation, and its corresponding chemical potential as a function of temperature and pressure. q, ε_{VBM}, $\Delta\varepsilon$, and IP are the effective charge of the defect, the valence band edge, a correction for shift in the valence band edge due to the jellium background for charged defects, and the ionization energy. T and p have their usual meanings. $\Delta_f G_{def}^{vib}$ is calculated as the difference in the temperature dependence of the free energy between a supercell containing a defect and a perfect supercell of the same size. Since the enthalpy exhibits weak temperature dependence, this term is dominated by the vibrational entropy contribution at all considered temperatures. For the gaseous species, $\mu_i(T,p)$ is obtained from the DFT energy, E^{DFT}, and tabulated values for the zero point energy, E_i^{ZP}, temperature dependence of the enthalpy, $H_i^{\circ}(T)$, and entropy, $S_i^{\circ}(T)$,

$$\mu_i = E^{DFT} + E_i^{ZP} + H_i^{\circ}(T) - TS_i^{\circ}(T) + k_B T \ln\left(\frac{p_i}{p^{\circ}}\right) \quad (3)$$

as standard DFT fails in predicting the correct binding energy of small molecules, we rather use the DFT energy of isolated atoms and experimental binding energies.

From the free energy of defect formation, the equilibrium defect concentration in bulk, c_i, is determined according to

$$\frac{c_i}{c_s - c_i - c_d} = \exp\left(-\frac{\Delta_f G_i^{\circ}}{k_B T}\right) \quad (4)$$

where c_s is the concentration of regular particles on lattice site s and c_d is the concentration of all other defects that form on the same lattice site s. Furthermore, the electrostatic potential difference across the interface, Φ, is obtained from the bulk-to-bulk segregation energies and bulk defect concentrations

$$\Phi = \frac{1}{q_i}\left[(\Delta\mu^{\circ,seg}) + k_B T \ln\left(\frac{c'_{i,bulk}[c_s - c_{i,bulk}]}{c_{i,bulk}[c'_s - c'_{i,bulk}]}\right)\right] \quad (5)$$

where $\Delta\mu^{\circ,seg} = \mu_i^{\circ} - \mu_i^{\circ\prime}$ is the difference in the chemical potential of a defect in the two materials, i.e., the segregation energy of the defect from one phase to the other, and $c_{i,bulk}$ is the concentration of defect i. The prime denotes a different phase. More details can be found in ref 23.

The concentration of defects as a function of distance from the interface is obtained from the relation

$$c_i(x) = \frac{(c_s - c_d(x))c'_{i,bulk}\exp\left(-\frac{\Delta\mu^{\circ,seg}}{k_B T} - \frac{q_i\Delta\varphi(x)}{k_B T}\right)}{c'_s - c'_{i,bulk} - c'_{d,bulk} - c'_{i,bulk}\exp\left(-\frac{\Delta\mu^{\circ,seg}}{k_B T} - \frac{q_i\Delta\varphi(x)}{k_B T}\right)} \quad (6)$$

where $\Delta\varphi(x) = \varphi(0) - \varphi(x)$ is the difference in the electrostatic potential at a distance x from the interface relative to that at the interface; it is found by solving Poisson's equation, which expresses the difference in electrostatic potential in terms of the charge density, $\rho(x)$:

$$\frac{d^2}{dx^2}\Delta\varphi(x) = -\frac{\rho(x)}{\epsilon} \quad (7)$$

with the boundary conditions

$$\frac{d}{dx}\varphi(x) = 0\Big|_{x=\pm\infty} \quad (8)$$

and

$$\varepsilon\frac{d}{dx}\varphi(x) = -\varepsilon'\frac{d}{dx'}\varphi(x')\Big|_{x=x'=0} \quad (9)$$

For a complete description of the thermodynamics, the reader is referred to ref 23.

RESULTS AND DISCUSSION

Bulk Defect Chemistry. The two constituents, $BaZrO_3$ and $SrTiO_3$, exhibit different bulk defect chemistries, depending on doping type and level, temperature, and atmospheric conditions, which, in turn, control their interface defect chemistry. The most important defect reactions in the present system are the hydration reaction

$$H_2O(g) + v_O^{\bullet\bullet} + O_O^{\times} \rightleftharpoons 2OH_O^{\bullet} \quad (10)$$

which determines the relative concentrations of $v_O^{\bullet\bullet}$ and $OH_O^{\bullet}$, and the reduction reaction of $SrTiO_3$

$$2Ti_{Ti}^{\times} + O_O^{\times} \rightleftharpoons \frac{1}{2}O_2(g) + v_O^{\bullet\bullet} + 2Ti'_{Ti} \quad (11)$$

which results in formation of electrons localized on the Ti-site (Ti'_{Ti}) and $v_O^{\bullet\bullet}$ in $SrTiO_3$ at elevated temperatures and reducing atmospheres. Reduction of acceptor-doped $BaZrO_3$ is insignificant and therefore not considered. The calculated hydration enthalpies of $BaZrO_3$ and $SrTiO_3$ are −0.81 and −0.29 eV, respectively, in line with previous computational and experimental studies.[5,33−35] The reduction enthalpy, ΔH_{red}, according to eq 11, is calculated to be 6.2 eV, which is similar to the experimentally reported value of 6.1 eV.[36] A delocalized electron results in a similar reduction enthalpy (6.15 eV), but lower entropy. At 1000 K, the calculated vibrational entropy for the localized electron is 40 J/(mol K), which results in a contribution to the free energy of 0.41 eV. This value is low compared to the enthalpy, suggesting that treating the electrons as localized states, as we do in this work, will not have a significant influence on the following discussion. In addition to the defects included in eqs 10 and 11, we have considered cation vacancies (notably Sr and Ba vacancies), which may form during high temperature fabrication. The concentrations of cation vacancies are assumed frozen-in below 1200 K. Before evaluating the interface defect properties, we consider the bulk defect chemistry with various types of homogeneous doping. Figure 2 shows the defect structure of acceptor-doped $BaZrO_3$ and undoped and donor-doped $SrTiO_3$ as a function of inverse temperature under wet, reducing conditions. Below 800 °C, $OH_O^{\bullet}$ is the majority defect in acceptor-doped $BaZrO_3$ under wet conditions, independent of the oxygen partial pressure. On the other hand, in undoped $SrTiO_3$, the defect chemistry is dominated by $v_O^{\bullet\bullet}$ that is charge-compensating the constant (frozen-in) concentration of v''_{Sr} below 500 °C, and an increasing concentration of electrons, Ti'_{Ti}, above. $OH_O^{\bullet}$ is in minority under all practical conditions in both undoped and donor-doped $SrTiO_3$. In donor-doped $SrTiO_3$, the dopant is compensated by Ti'_{Ti} below 900 °C,

https://dx.doi.org/10.1021/acs.jpcc.0c00385
J. Phys. Chem. C 2020, 124, 14072−14081

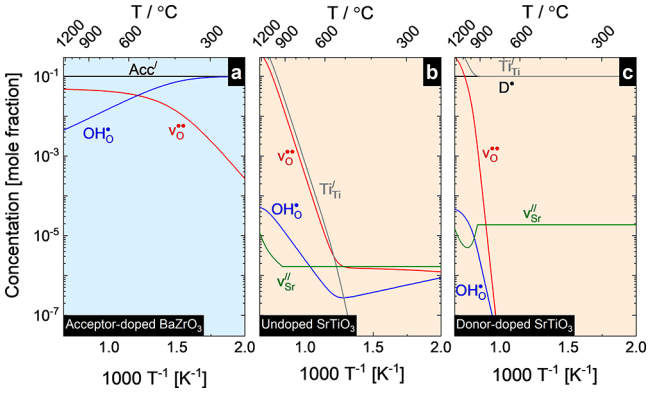

Figure 2. Defect concentration as a function of inverse temperature in (a) acceptor-doped $BaZrO_3$, (b) undoped $SrTiO_3$, and (c) donor-doped $SrTiO_3$ in wet, reducing atmosphere p_{H_2O} = 0.03 bar and p_{O_2} = 10^{-30} bar).

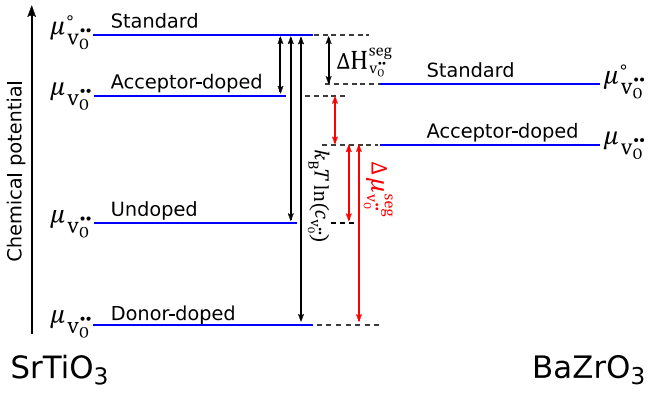

Figure 3. Schematic representation of the standard chemical potential of $v_O^{\bullet\bullet}$, the change in chemical potential with doping, and its influence on the segregation energy of defects.

above which further reduction of Ti ions results in an electroneutrality dominated by Ti'_{Ti} and $v_O^{\bullet\bullet}$.

Electron holes dominate the electrical conductivity in acceptor-doped $BaZrO_3$ and $SrTiO_3$ at high temperatures and oxygen partial pressures[37,38] and are as such important to consider. However, in undoped and donor-doped $SrTiO_3$, the concentrations of electron holes are low, and they are therefore omitted from Figure 2 and in further calculations. In general, the concentration profile of electron holes follows that of protons near the interface.

Interface Defect Chemistry. *Segregation Thermodynamics.* The defect structure and electrostatic potential difference at a heterogeneous epitaxial interface are largely governed by the chemical potential of the charged species in the two bulk phases, and can be described by a set of heterogeneous defect reactions such as

$$O^{\times}_{O,BaZrO_3} + v^{\bullet\bullet}_{O,SrTiO_3} = v^{\bullet\bullet}_{O,BaZrO_3} + O^{\times}_{O,SrTiO_3} \quad (12)$$

The direction and extent of reaction 12 is determined by the difference in the chemical potential of defects in the two phases, composed of a standard material specific component and a configurational component. The standard chemical potential reflects the chemical properties of the material and its affinity for specific defects/chemical species. For a given material it can, however, be tuned somewhat through strain.[23] The activity component is, on the other hand, given by the concentration of defects and may be tuned by homogeneous doping and changes in external parameters such as temperature and atmospheric conditions.

Figure 3 illustrates the relationship between the standard chemical potentials, standard segregation energy ($\Delta\mu^{\circ,seg}$), and contribution from the configurational part to the overall segregation energy ($\Delta\mu^{seg}$) of a species. The figure shows the effect of homogeneous doping on the segregation energy of defects (by pinning their chemical potential in the bulk) and, hence, the electrostatic potential difference between the two phases. Although $v_O^{\bullet\bullet}$ is used for illustration in eq 12 and Figure 3, the principle applies to all other defects and combinations of materials.

In the current system, $\mu^{\circ,seg}$ for segregation of $v_O^{\bullet\bullet}$ and $OH_O^{\bullet}$ from $SrTiO_3$ to $BaZrO_3$ are −0.64 and −0.56 eV, respectively, and reaction 12 thus proceeds in the direction it is written. Upon doping, the concentration term affects the segregation energy ($\Delta\mu^{seg}$), which for undoped, acceptor-doped, or donor-doped $SrTiO_3$ in contact with acceptor-doped $BaZrO_3$ becomes −0.02, −0.52, or 2.81 eV for $v_O^{\bullet\bullet}$ at 600 K, respectively. Consequently, the electrostatic potential difference across the interface, Φ, is also affected by doping as it is closely related to the difference in chemical potential (eq 5) and serves to limit the extent of defect segregation. Homogeneous doping as such significantly affects Φ and the defect chemistry of the interface, and the direction of defect segregation according to reaction 12 may even be reversed by homogeneous doping of $BaZrO_3$ and $SrTiO_3$ with acceptors and donors, respectively. While homogeneous doping affects the configurational part of the segregation energy, $\Delta\mu^{\circ,seg}$ is material dependent. Replacing $SrTiO_3$ by for instance $BaTiO_3$ or $BaCeO_3$ in contact with $BaZrO_3$ changes the standard segregation energy of $v_O^{\bullet\bullet}$ from −0.64 to −0.61 or +0.36 eV, respectively. For $OH_O^{\bullet}$, $\Delta\mu^{\circ,seg}$ changes from −0.56 to −0.46 or +0.50 eV, respectively. Thus, the direction of such defect segregation—and the nature and extent of the heterogeneous doping effect—at a heterointerface can be reversed through the choice of materials, although homogeneous doping has a far greater effect on the interface defect chemistry. Lastly, as discussed in our previous work on the topic, strain at the interface affects the chemistry of the two materials and as such the segregation energies and interface defect chemistry and represents yet another degree of freedom in tailoring the defect chemical properties of heterointerfaces.[23]

Figure 4 summarizes the calculated electrostatic potential differences, Φ, across the interface between acceptor-doped $BaZrO_3$ and undoped, donor-doped, and acceptor-doped $SrTiO_3$ as a function of temperature under reducing conditions. At the highest temperatures (i.e., above 1300 K), Φ is essentially independent of the homogeneous doping type in $SrTiO_3$ as a consequence of the dominance of intrinsic defects (i.e., electrons and oxygen vacancies) under sufficiently reducing conditions. In the extrinsically dominated regime, however, Φ, and as such the interface defect chemistry, strongly depends on the type of homogeneous dopant in $SrTiO_3$ with Φ ranging from negative values for undoped and acceptor-doped $SrTiO_3$ to highly positive for donor-doped $SrTiO_3$.

In the following sections, we proceed by, first, exploring the interfacial defect chemistry at the epitaxial $SrTiO_3$ and $BaZrO_3$ interface within two limiting homogeneous doping situations in more detail, i.e., undoped vs donor-doped $SrTiO_3$ (as opposed to the acceptor-doped $SrTiO_3$ vs acceptor-doped

https://dx.doi.org/10.1021/acs.jpcc.0c00385
J. Phys. Chem. C 2020, 124, 14072−14081

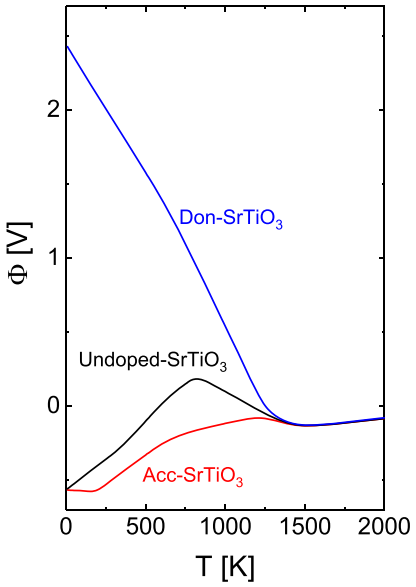

Figure 4. Electrostatic potential across the interface between acceptor-doped $BaZrO_3$ and acceptor-doped, undoped, or donor-doped $SrTiO_3$ as a function of temperature in wet, reducing atmosphere (p_{H_2O} = 0.03 bar and p_{O_2} = 10^{-30} bar).

$BaZrO_3$ situation discussed in ref 23), and, second, by discussing the potential implications of heterogeneously doped oxide nanocomposites in electrochemical applications.

Undoped $SrTiO_3$/Acceptor-Doped $BaZrO_3$. As shown in Figure 4, at the interface of undoped $SrTiO_3$ and acceptor-doped $BaZrO_3$, Φ changes its sign from negative to positive upon increasing temperature and reaches a maximum at 800 K. This temperature dependence stems from the configurational term in the expression of Φ (eq 5), which dominates due to the large difference in the concentrations of $v_O^{\bullet\bullet}$ and $OH_O^{\bullet}$ between $SrTiO_3$ and $BaZrO_3$. Below 800 K, undoped $SrTiO_3$ is dominated by $v_O^{\bullet\bullet}$ that charge-compensate frozen-in v_{Sr}'' (the same applies to materials with frozen-in extrinsic acceptor impurities), and the concentration of $v_O^{\bullet\bullet}$ is largely temperature independent. In acceptor-doped $BaZrO_3$, $OH_O^{\bullet}$ is, on the other hand, the majority positive defect, rendering the minority concentration of $v_O^{\bullet\bullet}$ strongly temperature dependent. At the very lowest temperatures, $OH_O^{\bullet}$ replaces $v_O^{\bullet\bullet}$ as the dominant defect in undoped $SrTiO_3$, which thus dictates Φ as reflected in the bend in the electrostatic potential curve below 200 K.

Above 800 K, $SrTiO_3$ reverts to the intrinsic defect regime in which $v_O^{\bullet\bullet}$ and charge-compensating Ti_{Ti}' dominate concentration-wise, while the concentration of $v_O^{\bullet\bullet}$ in $BaZrO_3$ is limited by the constant acceptor concentration. Thus, in this temperature range, Φ is governed by the temperature dependence of the concentration of oxygen vacancies in $SrTiO_3$, which in turn is given by the reduction thermodynamics of $SrTiO_3$.

At 600 K, the electrostatic potential difference between the two materials is 0 V. Although the direction of defect segregation is reversed, such a low potential difference does not affect the concentrations of defects near the interface. At 900 K, however, the electrostatic potential difference becomes significantly higher, 0.15 V, and—in combination with higher defect concentration in the bulk of $SrTiO_3$—results in a substantial space-charge effect. Figure 5 displays the defect concentration and resulting electrostatic potential profiles across the interface at 900 K in wet, reducing atmosphere calculated in the Mott−Schottky approximation. In $BaZrO_3$, the electrostatic potential results in a space-charge layer depleted of $v_O^{\bullet\bullet}$ and $OH_O^{\bullet}$, with a thickness of less than 1 nm. The low defect concentrations in the bulk of $SrTiO_3$ lead to a space-charge layer that extends to more than 50 nm. Yet, the majority of charge accumulation occurs near the interface, where the concentration of $v_O^{\bullet\bullet}$ is enhanced by 2 orders of magnitude, while those of protons and electron holes are enhanced by 1 order of magnitude.

Although the absolute value of the electrostatic potential difference is similar for the current interface compared to that where both $SrTiO_3$ and $BaZrO_3$ are 10 mol % acceptor-doped (0.15 vs −0.14 V), the charge depleted (or accumulated) is significantly lower (0.017 vs 0.23 C/m^2 of interface area), which is another consequence of the low defect concentration in bulk $SrTiO_3$. As such, a substantially higher electrostatic potential difference is needed in order to bring about larger spatial separation of transporting and charge-compensating (i.e., dopants) defects in the two materials.

Albeit the amount of charge redistribution at this specific interface is rather limited, it illustrates the potential of heterogeneous doping of a nominally undoped material through spatial separation of charge-compensating defects at heterointerfaces, and that the direction of defect segregation can be manipulated by the type of homogeneous doping. The effect would be significantly stronger at heterointerfaces where the standard segregation thermodynamics favors defect

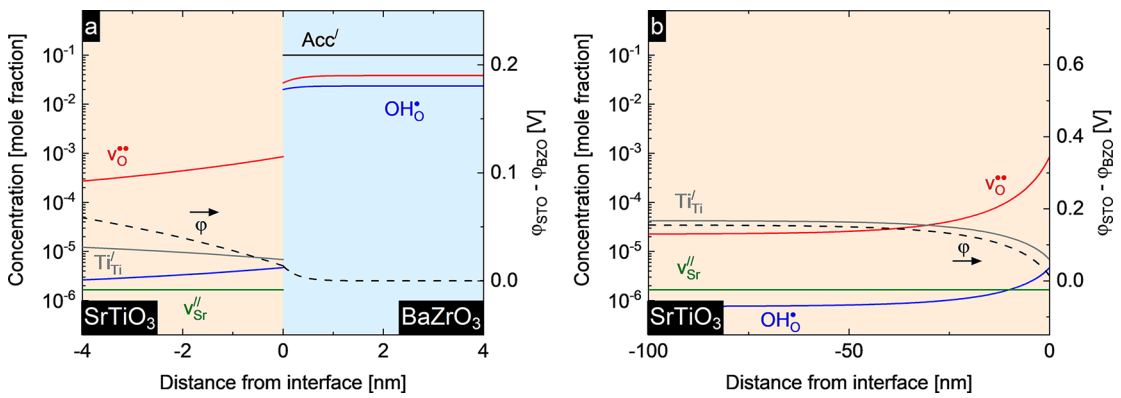

Figure 5. Electrostatic potential and defect concentration profiles across the interface between undoped $SrTiO_3$ and acceptor-doped $BaZrO_3$ (a) and the full profiles in $SrTiO_3$ (b) at 900 K in wet, reducing atmosphere (p_{H_2O} = 0.03 bar and p_{O_2} = 10^{-30} bar).

https://dx.doi.org/10.1021/acs.jpcc.0c00385
J. Phys. Chem. C 2020, 124, 14072−14081

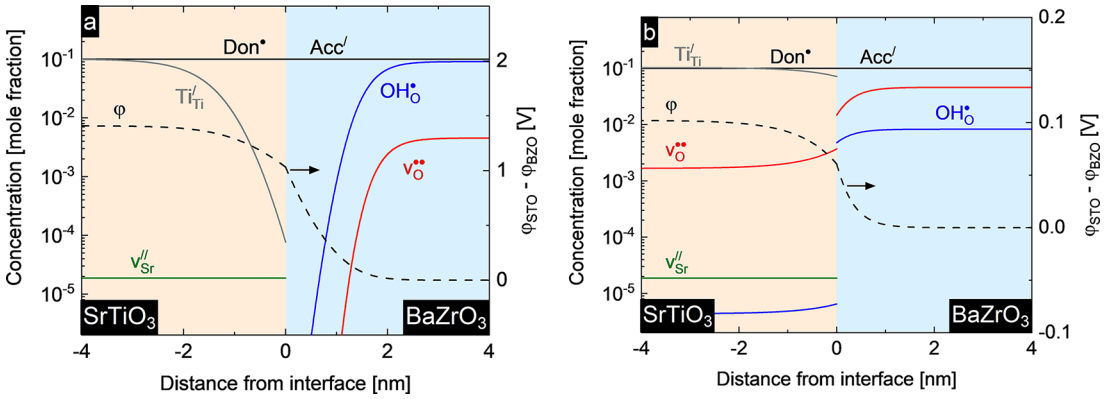

Figure 6. Electrostatic potential and defect concentration profiles across the interface between $SrTiO_3$ and $BaZrO_3$ at (a) 600 and (b) 1200 K in wet, reducing atmosphere (p_{H_2O} = 0.03 bar and p_{O_2} = 10^{-30} bar).

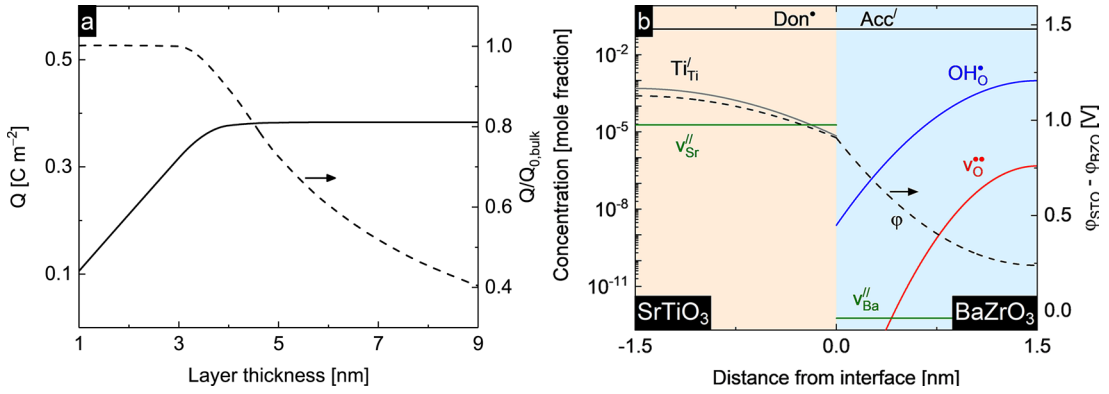

Figure 7. Amount of charge stored at the interface and the ratio of stored charge and initial charge in the layers as a function of layer thickness in a multilayered thin film (a) and electrostatic potential and defect concentration profiles across the interface between donor-doped $SrTiO_3$ and acceptor-doped $BaZrO_3$ as a function of distance from the interface (b) at 600 K under wet, reducing conditions.

segregation to the undoped material. As such, a significant heterogeneous doping effect may be achieved even in undoped materials despite the low defect concentration in their bulk.

Donor-Doped $SrTiO_3$/Acceptor-Doped $BaZrO_3$. Homogenous donor-doping strongly affects the chemical potential of oxygen vacancies and protons in $SrTiO_3$ at lower temperatures (Figure 2) and as such the direction and extent of defect segregation at the interface to acceptor-doped $BaZrO_3$. As shown in Figure 4, Φ is highly positive at the lowest temperatures, and decreases with increasing temperature due to the small and increasing minority concentration of $v_O^{\bullet\bullet}$ in $SrTiO_3$ below ~1300 K. Above ~1300 K, Φ reverses its sign due to the transition to the intrinsically dominated defect regime which in turn reverses the direction of defect segregation at the interface.

Figure 6 shows an example of the defect chemistry at an interface of donor-doped $SrTiO_3$ and acceptor-doped $BaZrO_3$ at 600 and 1200 K under wet, reducing conditions. At 600 K, the electrostatic potential difference across the interface is 1.41 V, which is significantly higher than at grain boundaries and surfaces of perovskites,[39−41] and stems from the large difference in the chemical activity of $v_O^{\bullet\bullet}$ and $OH_O^{\bullet}$ in $SrTiO_3$ and $BaZrO_3$. This in turn leads to significantly depleted space-charge layers on both sides of the interface; while $BaZrO_3$ is depleted of $v_O^{\bullet\bullet}$ and $OH_O^{\bullet}$ near the interface, $SrTiO_3$ is depleted of the majority Ti_{Ti}' (and enriched by the minority $v_O^{\bullet\bullet}$ and $OH_O^{\bullet}$). The positive charge in $SrTiO_3$ is however mainly due to depletion of Ti_{Ti}' rather than enrichment of $v_O^{\bullet\bullet}$ due to the low concentration of $v_O^{\bullet\bullet}$ relative to that of Ti_{Ti}' in the bulk material. In $BaZrO_3$, charge compensation proceeds through depletion of the majority defect, $OH_O^{\bullet}$. The resulting space-charge-layer width is 3 nm in $SrTiO_3$, and is somewhat smaller in $BaZrO_3$ due to its smaller dielectric constant.

At 1200 K (Figure 6b), Φ is significantly smaller (0.10 V) leading to weaker depletion and narrower (1 nm) space-charge regions compared to the low temperature case. Moreover, a significant enrichment of $v_O^{\bullet\bullet}$ near the interface results in somewhat weaker depletion of Ti_{Ti}' in $SrTiO_3$, which is a consequence of the more significant concentration of $v_O^{\bullet\bullet}$ at these temperatures. In $BaZrO_3$, both $v_O^{\bullet\bullet}$ and $OH_O^{\bullet}$ are depleted, though the former depletes steeper toward the interface due to its double charge.

The interfaces of both undoped, acceptor-doped, or donor-doped $SrTiO_3$ and acceptor-doped $BaZrO_3$ as such all exhibit significant nonstoichiometries that differ depending on the dominating defect disorder of the bulk materials. Whether defects accumulate or deplete near the interface is dependent on the bulk chemistry (i.e., defect/ion affinity) and doping type and level. As demonstrated for the interface between donor-doped $SrTiO_3$ and acceptor-doped $BaZrO_3$ at 1200 K, in situations where oppositely charged defects are present in significant amounts in one material, the accumulation and depletion of both defects would be limited. Moreover, a significant difference in the defect concentration across the interface results in larger Φ and, thus, represents a means to

https://dx.doi.org/10.1021/acs.jpcc.0c00385
J. Phys. Chem. C 2020, 124, 14072−14081

tailor the interface defect chemistry through varying the doping type and level in the constituent materials.

In general, interfaces between donor-doped and acceptor-doped materials will be characterized by formation of a depletion layer, in which defects on both sides of the interface are depleted, while interfaces between materials with the same doping type (i.e., both acceptor doped and donor doped) will be characterized by defect depletion on one side of the interface and enrichment on the other side. In the case where one or both materials are undoped, the situation at the interface falls in one of the aforementioned categories, dependent on whether the bulk is effectively donor- or acceptor-doped.

Size Effect. Interfacial effects may become decisive and cause transport and storage anomalies in mesoscopic systems where the particle size is of the same order as the space-charge-layer width. For instance, in acceptor-doped nanocrystalline CeO_2, the macroscopic electrical conductivity is n-type due to enrichment of electrons in the space-charge zone,[42] although a typical polycrystalline CeO_2 specimen is mixed p-type and $v_O^{\bullet\bullet}$ conductor.[43,44] As long as the space-charge layers do not overlap, the depleted (accumulated) charge near the interface is independent of particle size, except for increased interface-to-bulk volume ratio. However, in situations where the space-charge layers overlap, the concentrations in the particles centers are affected and eventually become proportional to the particle size, as shown for the interface of donor-doped $SrTiO_3$ and acceptor-doped $BaZrO_3$ in Figure 7a. For the donor-doped system, the space-charge layers dominate even in the center of the two phases when the particle size becomes smaller than 4 nm. Due to depletion of defects in both materials, the situation corresponds to an electroneutrality where donors in $SrTiO_3$ are charge-compensated by acceptors in $BaZrO_3$. Figure 7b shows the defect concentration and electrostatic potential profiles as a function of distance from the interface in a multilayered thin film with a layer thickness of 3 nm. The concentration of electrons in the center of the $SrTiO_3$ layer is more than 2 orders of magnitude lower than in the interior of macroscopic particles. The situation is similar in $BaZrO_3$, except that the concentrations of $v_O^{\bullet\bullet}$ and $OH_O^{\bullet}$ are significantly lower close to the interface.

As such, reducing the particle size to a few nanometers may be beneficial for the purpose of mass exchange as the entire particle contributes to charge storage. For the purpose of composite electrodes or gas separation membranes, on the other hand, small particle size would have a negative impact due to the substantial decrease in the concentration of mobile defects.

Mass/Charge Storage in Oxide Composites. As elaborated upon in the preceding sections, external factors such as temperature and atmospheric composition affect the electrostatic potential difference and, hence, the nonstoichiometry at heterointerfaces. Thus, a change in these parameters may result in reversible mass exchange with the surroundings, which in turn corresponds to reversible mass storage. Moreover, such mass exchange may also enable hydrogen production through thermochemical splitting of H_2O. In the donor-doped system, Figure 6, the depleted $OH_O^{\bullet}$ in $BaZrO_3$ is charge-compensated by depletion of Ti'_{Ti} in $SrTiO_3$, which results in release of H_2 upon, for instance, a decrease in the temperature. Thus, in this sense, higher electrostatic potential across the interface is beneficial as more mass can be depleted (i.e., more charge stored) near the interface; hence more H_2 can be released. At 600 K, the stored charge is 0.38 C/m^2 of interface: assuming a similar interface area as the surface area in some mesoporous oxides (i.e., 3000 m^2/g[45]) and a stored charge of 0.4 C/m^2 of interface, a hydrogen amount of 0.63% of the mass of the composite is stored.

Figure 8 shows the total stored charge and electrostatic potential on each side of the interface, as well as the charge due

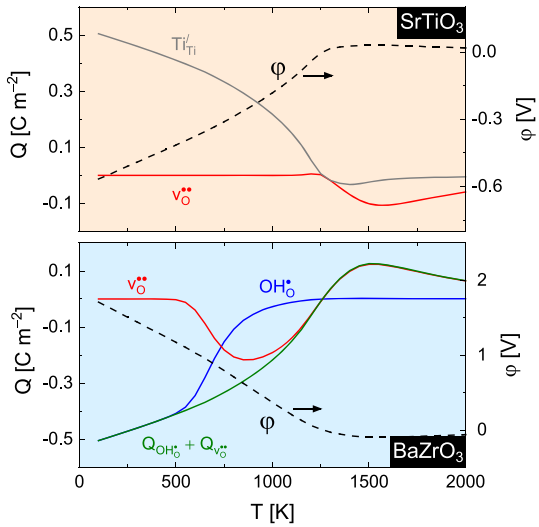

Figure 8. Charge stored near and electrostatic potential on each side of the interface between donor-doped $SrTiO_3$ and acceptor-doped $BaZrO_3$ as a function of temperature.

to different species, as a function of temperature. Below 600 K, charge exceeding 0.38 C/m^2 of interface area, increasing with decreasing temperature, is stored as depleted $OH_O^{\bullet}$ in $BaZrO_3$ and compensated by depletion of Ti'_{Ti} in $SrTiO_3$. In this temperature region, an amount of H_2 that corresponds to the difference in the stored charge is released when the temperature is lowered and incorporated when the temperature is raised. Above 700 K, dehydration of $BaZrO_3$ results in lower $OH_O^{\bullet}$ storage. However, under wet conditions and low oxygen partial pressure, depletion of $v_O^{\bullet\bullet}$ results in uptake of O from H_2O, which thus results in release of H_2. As such, as long as $SrTiO_3$ is dominated by Ti'_{Ti}, the total charge stored in $BaZrO_3$ can result in H_2 release, regardless of which of the two defects (i.e., $v_O^{\bullet\bullet}$ and $OH_O^{\bullet}$) dominates. The job-sharing reactions that occur at low and high temperature, respectively, are

$$OH^{\bullet}_{O,BaZrO_3} + Ti'_{Ti,SrTiO_3} = O^{\times}_{O,BaZrO_3} + Ti^{\times}_{Ti,,SrTiO_3} + \frac{1}{2}H_2(g) \quad (13)$$

and

$$v^{\bullet\bullet}_{O,BaZrO_3} + 2Ti'_{Ti,SrTiO_3} + H_2O(g) = O^{\times}_{O,BaZrO_3} + 2Ti^{\times}_{Ti,SrTiO_3} + H_2(g) \quad (14)$$

On cooling under wet, inert conditions, the job-sharing processes are reversed and result in release of O_2 instead:

$$O^{\times}_{O,BaZrO_3} + 2Ti^{\times}_{Ti,SrTiO_3} = v^{\bullet\bullet}_{O,BaZrO_3} + 2Ti'_{Ti,SrTiO_3} + \frac{1}{2}O_2(g) \quad (15)$$

https://dx.doi.org/10.1021/acs.jpcc.0c00385
J. Phys. Chem. C 2020, 124, 14072−14081

and

$$2O^{\times}_{O,BaZrO_3} + 2Ti^{\times}_{Ti,,SrTiO_3} + H_2O(g) = 2OH^{\bullet}_{O,BaZrO_3} + 2Ti'_{Ti,SrTiO_3} + \frac{1}{2}O_2(g) \quad (16)$$

at high and low temperatures, respectively.

Equations 13−16 show how mass storage through heterogeneous reactions can be utilized to conduct thermochemical H_2O splitting. In a sense, the process is similar to thermochemical H_2O splitting by reducible oxides such as CeO_2, where thermal reduction at high temperature is followed by reoxidation in H_2O to produce H_2,[46−49] except that it proceeds in the opposite direction. Unlike traditional thermochemical H_2O splitting, the process proposed here produces hydrogen upon heating due to the endothermic nature of oxidation in the space-charge layer as indicated by the increased concentration of Ti^{3+} at lower temperature in Figure 8. Moreover, since reactions 13−16 occur due to the change in Φ, which affects the defect concentrations within the space-charge layers, the process may be considered thermo-electrochemical, where the electrical potential is built in. In fact, an external electrical potential at the current interface can be used to shift reactions 13−16 forward. Further, H_2O splitting by heterostructures has several advantages compared to reducible oxides, since a nanostructured composite can exhibit significantly higher redox capacity, and it is possible to tailor the redox thermodynamics, by for instance choice of materials, to conduct the process at a specific temperature range. In addition, exchange of hydrogen at low temperatures exhibits faster kinetics than oxygen, which thus lowers the operation temperature and as such allows utilization of waste heat from other industrial processes for production of H_2 and O_2.

Implications for Electrochemical Applications. Ideally, the electrodes in electrochemical devices such as fuel cells and electrolyzers should exhibit mixed ionic and electronic conductivities (or transport of neutral species as illustrated in Figure 9a, left-hand side), which is challenging to achieve as good electron conductors usually suffer from poor ionic transport, whereas good ion conductors typically exhibit too low electronic conductivity. For instance Ni, which is widely used as negative electrode (negatrode) in proton ceramic electrochemical cells (PCEC), has good electronic conductivity and catalytic properties; however, due to its low hydrogen solubility, incorporation of H_2 into the electrolyte mainly occurs at the three-phase boundary (TPB) as illustrated in Figure 9a, right-hand side. Therefore, application of porous and/or composite electrodes has been necessary to enhance the performance of such electrodes through increasing the length of TPB, although sintering of the metal and coking when hydrocarbons are used as fuel lower the performance. Replacing the metal with an oxide could overcome these issues, and upon nanostructuring may give composite electrodes that mimic mixed conductors as illustrated in Figures 1a and 9. However, as predicted by our calculations on donor-doped $SrTiO_3$ and acceptor-doped $BaZrO_3$, there will be a depletion layer at the interface between an n-type conductor and an ionic or mixed p-type and ionic conductor, similar to that at p−n junctions in semiconductors. Formation of such a depletion layer limits the performance of donor-doped oxides as single-phase electrodes in fuel cells and electrolyzers; in both applications, charge-carrier depletion in the electrolyte reduces the current density, which thus increases the electrode resistance. For the same reason, the conductivity of oxide (nano)composites is lowered, making such composites unsuitable as negatrodes or hydrogen separation membranes. This conclusion is in line with hydrogen flux and electrical conductivity measurement performed on composites of Nb-doped $SrTiO_3$ and Y-doped $BaZrO_3$ that showed lower hydrogen permeation than predicted from the proton conductivity of $BaZrO_3$ and significantly lower total electrical conductivity than in single phase Nb-doped $SrTiO_3$.[50]

The situation reported for composites of Li_2O and Ru—where accumulation of H^+ and e^- or H^- occurs on either side of the interface—may be challenging to achieve in oxide composites (Figure 1b), which usually exhibit small oxygen deficiencies when dominated by electrons, causing the configurational term in the electrostatic potential to be substantial, typically 2−3 V. In order for both electrons and positively charged defects to accumulate on either side of the interface, the segregation energy of defects from the electron conductor to the ion conductor has to exceed the potential arising from the configurational term.

Although nanostructuring may not be promising for negatrodes, the situation is opposite for positive electrodes (positrodes), where both the electronic and ionic conductors are p-type. In that case, accumulation of defects on one side of the interfaces is charge-compensated by depletion on the other side. Since electron holes usually exhibit mobilities orders of magnitude higher than those of $v_O^{\bullet\bullet}$ and $H_i^{\bullet}$, a composite positrode may be constructed from materials that lead to accumulation of ionic defects in the ion conductor side of the interface at the expense of depletion of electron holes on the electronic conductor side of the interface. Acceptor-doped $SrTiO_3$, which is a moderate electron hole conductor under oxidizing conditions, and acceptor-doped (or undoped) $BaZrO_3$ (i.e., proton conductor)[23] fit this criteria and could potentially enable such nanocomposite positrodes.

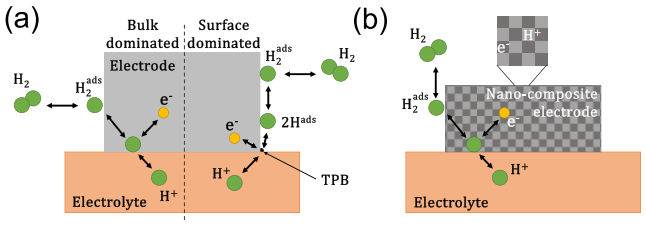

Figure 9. Illustration of H_2 splitting and subsequent incorporation into or diffusion at the surface of the metal (a) and at a nanocomposite of proton and ion conductors where space-charge overlap results in a situation similar to that in ideal electrodes (b).

CONCLUSIONS

The defect chemistry of heterogeneous interfaces between oxides has been addressed, and our results demonstrate that, in addition to the relative stability of defects, doping type and level have significant impacts on the interface defect structure. Interfaces between donor- and acceptor-doped oxides are expected to have a region where both materials are depleted for charge carriers at lower temperatures. On the other hand, interfaces between materials with the same doping type are expected to exhibit depletion of defects in one phase and enrichment in the other. First-principles calculations on a model system of $SrTiO_3$ and acceptor-doped $BaZrO_3$ show

https://dx.doi.org/10.1021/acs.jpcc.0c00385
J. Phys. Chem. C 2020, 124, 14072−14081

that $OH_O^{\bullet}$ and $v_O^{\bullet\bullet}$ segregate from $BaZrO_3$ to donor-doped and undoped $SrTiO_3$, although the standard energy for segregation of these defects from $BaZrO_3$ to $SrTiO_3$ is positive. The segregation is a result of the large difference in the activity of these defects across the interface when doping type in $SrTiO_3$ is changed. The number of defects segregating to undoped $SrTiO_3$ is somewhat low, yet it shows that decoupling of charge-compensating and transporting species, which eliminates association effects on defect transport, can be achieved. Reversing the doping situation—i.e., for the interface between undoped $BaZrO_3$ and acceptor-doped $SrTiO_3$—results in a significant enrichment of protons in $BaZrO_3$, which in a nanocomposite causes the total concentration of mobile defects in $BaZrO_3$ to be similar to that in $SrTiO_3$. In the case of donor-doped $SrTiO_3$, segregation of defects causes depletion of electrons and protons near the interface, which results in an overall change in the stoichiometry of the interface structure. Effectively, this results in reversible storage of H_2 upon, for instance, temperature cycling and thus allows H_2 and O_2 production through thermochemical splitting of H_2O. Depletion of charge carriers makes nanocomposites between oxide n-type conductors and proton/oxide ion conductors unsuitable as electrodes in electrochemical applications or hydrogen separation membranes.

AUTHOR INFORMATION

Corresponding Author

Tor S. Bjørheim − *Centre for Materials Science and Nanotechnology, Department of Chemistry, University of Oslo, FERMiO, NO-0349 Oslo, Norway;* orcid.org/0000-0002-5720-2784; Email: torsb@kjemi.uio.no

Authors

Sarmad W. Saeed − *Centre for Materials Science and Nanotechnology, Department of Chemistry, University of Oslo, FERMiO, NO-0349 Oslo, Norway;* orcid.org/0000-0002-5234-8573

Truls Norby − *Centre for Materials Science and Nanotechnology, Department of Chemistry, University of Oslo, FERMiO, NO-0349 Oslo, Norway*

Complete contact information is available at: https://pubs.acs.org/10.1021/acs.jpcc.0c00385

Notes

The authors declare no competing financial interest.

ACKNOWLEDGMENTS

The Norwegian Metacenter for Computational Science (NOTUR) is acknowledged for providing the computational resources under Project NN4604k.

REFERENCES

(1) Liang, C. C. Conduction characteristics of the lithium iodide-aluminum oxide solid electrolytes. *J. Electrochem. Soc.* **1973**, *120* (10), 1289−1292.

(2) Li, H.; Balaya, P.; Maier, J. Li-storage via heterogeneous reaction in selected binary metal fluorides and oxides. *J. Electrochem. Soc.* **2004**, *151* (11), A1878−A1885.

(3) Yu, X. Q.; Sun, J. P.; Tang, K.; Li, H.; Huang, X. J.; Dupont, L.; Maier, J. Reversible lithium storage in LiF/Ti nanocomposites. *Phys. Chem. Chem. Phys.* **2009**, *11* (41), 9497−9503.

(4) Balaya, P.; Li, H.; Kienle, L.; Maier, J. Fully reversible homogeneous and heterogeneous Li storage in RuO_2 with high capacity. *Adv. Funct. Mater.* **2003**, *13* (8), 621−625.

(5) Björketun, M. E.; Sundell, P. G.; Wahnström, G. Structure and thermodynamic stability of hydrogen interstitials in $BaZrO_3$ perovskite oxide from density functional calculations. *Faraday Discuss.* **2007**, *134* (0), 247−265.

(6) Yamazaki, Y.; Blanc, F.; Okuyama, Y.; Buannic, L.; Lucio-Vega, J. C.; Grey, C. P.; Haile, S. M. Proton trapping in yttrium-doped barium zirconate. *Nat. Mater.* **2013**, *12*, 647.

(7) Björketun, M. E.; Sundell, P. G.; Wahnström, G. Effect of acceptor dopants on the proton mobility in $BaZrO_3$: A density functional investigation. *Phys. Rev. B: Condens. Matter Mater. Phys.* **2007**, *76* (5), 054307.

(8) Saku, T.; Horikoshi, Y.; Tokura, Y. Limit of electron mobility in AlGaAs/GaAs modulation-doped heterostructures. *Jpn. J. Appl. Phys.* **1996**, *35*, 34−38.

(9) Gaska, R.; Shur, M. S.; Bykhovski, A. D.; Orlov, A. O.; Snider, G. L. Electron mobility in modulation-doped AlGaN−GaN heterostructures. *Appl. Phys. Lett.* **1999**, *74* (2), 287−289.

(10) Maier, J. Heterogeneous doping of silver bromide (AgBr:A-l_2O_3). *Mater. Res. Bull.* **1985**, *20* (4), 383−392.

(11) Lauer, U.; Maier, J. Conductivity enhancement and microstructure in AgCl/AgI composites. *Solid State Ionics* **1992**, *51* (3), 209−213.

(12) Yamada, H.; Bhattacharyya, A. J.; Maier, J. Extremely high silver ionic conductivity in composites of silver halide (AgBr, AgI) and mesoporous alumina. *Adv. Funct. Mater.* **2006**, *16* (4), 525−530.

(13) Guo, X. X.; Matei, I.; Lee, J. S.; Maier, J. Ion conduction across nanosized CaF_2/BaF_2 multilayer heterostructures. *Appl. Phys. Lett.* **2007**, *91* (10), 103102.

(14) Sata, N.; Jin-Phillipp, N. Y.; Eberl, K.; Maier, J. Enhanced ionic conductivity and mesoscopic size effects in heterostructures of BaF_2 and CaF_2. *Solid State Ionics* **2002**, *154−155*, 497−502.

(15) Maier, J. Nanoionics: Ion transport and electrochemical storage in confined systems. *Nat. Mater.* **2005**, *4* (11), 805−815.

(16) Maier, J. Mass storage in space charge regions of nano-sized systems: (Nano-ionics. Part V). *Faraday Discuss.* **2007**, *134*, 51−66.

(17) Fu, L.; Tang, K.; Oh, H.; Manickam, K.; Bräuniger, T.; Chandran, C. V.; Menzel, A.; Hirscher, M.; Samuelis, D.; Maier, J. Job-sharing" storage of hydrogen in Ru/Li_2O nanocomposites. *Nano Lett.* **2015**, *15* (6), 4170−4175.

(18) Garcia-Barriocanal, J.; Rivera-Calzada, A.; Varela, M.; Sefrioui, Z.; Iborra, E.; Leon, C.; Pennycook, S. J.; Santamaria, J. Colossal ionic conductivity at interfaces of epitaxial ZrO_2:Y_2O_3/$SrTiO_3$ heterostructures. *Science* **2008**, *321* (5889), 676−680.

(19) Foglietti, V.; Yang, N.; Tebano, A.; Aruta, C.; Di Bartolomeo, E.; Licoccia, S.; Cantoni, C.; Balestrino, G. Heavily strained $BaZr_{0.8}Y_{0.2}O_{3-x}$ interfaces with enhanced transport properties. *Appl. Phys. Lett.* **2014**, *104* (8), 081612.

(20) Yang, N.; Cantoni, C.; Foglietti, V.; Tebano, A.; Belianinov, A.; Strelcov, E.; Jesse, S.; Di Castro, D.; Di Bartolomeo, E.; Licoccia, S.; et al. Defective interfaces in yttrium-doped barium zirconate films and consequences on proton conduction. *Nano Lett.* **2015**, *15* (4), 2343−2349.

(21) De Souza, R. A.; Ramadan, A. H. H. Ionic conduction in the $SrTiO_3$|YSZ|$SrTiO_3$ heterostructure. *Phys. Chem. Chem. Phys.* **2013**, *15* (13), 4505−4509.

(22) Zarotti, F.; Felici, R.; Foglietti, V.; Liu, Z.; Yang, N.; Balestrino, G. Emerging proton conductivity at the interface between insulating $NdGaO_3$ and $BaZrO_3$. *Phys. Rev. Mater.* **2019**, *3* (10), 103606.

(23) Saeed, S. W.; Norby, T.; Bjørheim, T. S. Charge-carrier enrichment at $BaZrO_3/SrTiO_3$ interfaces. *J. Phys. Chem. C* **2019**, *123* (34), 20808−20816.

(24) Perdew, J. P.; Burke, K.; Ernzerhof, M. Generalized Gradient Approximation Made Simple. *Phys. Rev. Lett.* **1996**, *77* (18), 3865−3868.

(25) Kresse, G.; Hafner, J. Ab initio molecular-dynamics simulation of the liquid-metal–amorphous-semiconductor transition in germanium. *Phys. Rev. B: Condens. Matter Mater. Phys.* **1994**, *49* (20), 14251−14269.

(26) Kresse, G.; Furthmüller, J. Efficiency of ab-initio total energy calculations for metals and semiconductors using a plane-wave basis set. *Comput. Mater. Sci.* **1996**, *6* (1), 15−50.
(27) Kresse, G.; Furthmüller, J. Efficient iterative schemes for ab initio total-energy calculations using a plane-wave basis set. *Phys. Rev. B: Condens. Matter Mater. Phys.* **1996**, *54* (16), 11169−11186.
(28) Dudarev, S. L.; Botton, G. A.; Savrasov, S. Y.; Humphreys, C. J.; Sutton, A. P. Electron-energy-loss spectra and the structural stability of nickel oxide: An LSDA+U study. *Phys. Rev. B: Condens. Matter Mater. Phys.* **1998**, *57* (3), 1505−1509.
(29) Erhart, P.; Klein, A.; Åberg, D.; Sadigh, B. Efficacy of the DFT +U formalism for modeling hole polarons in perovskite oxides. *Phys. Rev. B: Condens. Matter Mater. Phys.* **2014**, *90* (3), 035204.
(30) Blöchl, P. E. Projector augmented-wave method. *Phys. Rev. B: Condens. Matter Mater. Phys.* **1994**, *50* (24), 17953−17979.
(31) Kresse, G.; Joubert, D. From ultrasoft pseudopotentials to the projector augmented-wave method. *Phys. Rev. B: Condens. Matter Mater. Phys.* **1999**, *59* (3), 1758−1775.
(32) Togo, A.; Tanaka, I. First principles phonon calculations in materials science. *Scr. Mater.* **2015**, *108*, 1−5.
(33) Kjølseth, C.; Wang, L.-Y.; Haugsrud, R.; Norby, T. Determination of the enthalpy of hydration of oxygen vacancies in Y-doped $BaZrO_3$ and $BaCeO_3$ by TG-DSC. *Solid State Ionics* **2010**, *181* (39), 1740−1745.
(34) Kreuer, K. D. Aspects of the formation and mobility of protonic charge carriers and the stability of perovskite-type oxides. *Solid State Ionics* **1999**, *125*, 285.
(35) Waser, R. Proton solubility in undoped and Fe-doped $SrTiO_3$: Temperature dependence and formation of defect associates. *Z. Naturforsch., A: Phys. Sci.* **1987**, *42* (11), 1357−1365.
(36) Moos, R.; Hardtl, K. H. Defect chemistry of donor-doped and undoped strontium titanate ceramics between 1000° and 1400°C. *J. Am. Ceram. Soc.* **1997**, *80* (10), 2549−2562.
(37) Bohn, H. G.; Schober, T. Electrical Conductivity of the High-Temperature Proton Conductor $BaZr_{0.9}Y_{0.1}O_{2.95}$. *J. Am. Ceram. Soc.* **2000**, *83* (4), 768−772.
(38) Shi, T.; Chen, Y.; Guo, X. Defect chemistry of alkaline earth metal (Sr/Ba) titanates. *Prog. Mater. Sci.* **2016**, *80*, 77−132.
(39) Kjølseth, C.; Fjeld, H.; Prytz, Ø.; Dahl, P. I.; Estournès, C.; Haugsrud, R.; Norby, T. Space−charge theory applied to the grain boundary impedance of proton conducting $BaZr_{0.9}Y_{0.1}O_{3-\delta}$. *Solid State Ionics* **2010**, *181* (5), 268−275.
(40) Nyman, B. J.; Helgee, E. E.; Wahnström, G. Oxygen vacancy segregation and space-charge effects in grain boundaries of dry and hydrated $BaZrO_3$. *Appl. Phys. Lett.* **2012**, *100* (6), 061903.
(41) Polfus, J. M.; Bjørheim, T. S.; Norby, T.; Bredesen, R. Surface defect chemistry of Y-substituted and hydrated $BaZrO_3$ with subsurface space-charge regions. *J. Mater. Chem. A* **2016**, *4* (19), 7437−7444.
(42) Chiang, Y. M.; Lavik, E. B.; Kosacki, I.; Tuller, H. L.; Ying, J. Y. Defect and transport properties of nanocrystalline CeO_{2-x}. *Appl. Phys. Lett.* **1996**, *69* (2), 185−187.
(43) Kilner, J. A. Fast oxygen transport in acceptor doped oxides. *Solid State Ionics* **2000**, *129* (1), 13−23.
(44) Gerhardt, R.; Nowick, A. S. Grain-boundary effect in ceria doped with trivalent cations: I, electrical measurements. *J. Am. Ceram. Soc.* **1986**, *69* (9), 641−646.
(45) Bera, B.; Das, N. Synthesis of high surface area mesoporous silica SBA-15 for hydrogen storage application. *Int. J. Appl. Ceram. Technol.* **2019**, *16* (1), 294−303.
(46) Abanades, S.; Flamant, G. Thermochemical hydrogen production from a two-step solar-driven water-splitting cycle based on cerium oxides. *Sol. Energy* **2006**, *80* (12), 1611−1623.
(47) Ishida, T.; Gokon, N.; Hatamachi, T.; Kodama, T. Kinetics of thermal reduction step of thermochemical two-step water splitting using CeO_2 particles: MASTER-plot method for analyzing non-isothermal experiments. *Energy Procedia* **2014**, *49*, 1970−1979.
(48) Bulfin, B.; Call, F.; Lange, M.; Lübben, O.; Sattler, C.; Pitz-Paal, R.; Shvets, I. V. Thermodynamics of CeO_2 thermochemical fuel production. *Energy Fuels* **2015**, *29* (2), 1001−1009.
(49) Chueh, W. C.; Falter, C.; Abbott, M.; Scipio, D.; Furler, P.; Haile, S. M.; Steinfeld, A. High-flux solar-driven thermochemical dissociation of CO_2 and H_2O using nonstoichiometric ceria. *Science* **2010**, *330* (6012), 1797−1801.
(50) Fish, J. S.; Ricote, S.; O'Hayre, R.; Bonanos, N. Electrical properties and flux performance of composite ceramic hydrogen separation membranes. *J. Mater. Chem. A* **2015**, *3* (10), 5392−5401.

https://dx.doi.org/10.1021/acs.jpcc.0c00385
J. Phys. Chem. C 2020, 124, 14072−14081